Direct comparison of [^{18}F]FDG brain images acquired from a phantom and patients using SiPM- and PMT-PET/CT

Kei Wagatsuma (wagatsuma@pet.tmig.or.jp)
Tokyo Metropolitan Institute of Gerontology https://orcid.org/0000-0001-7067-9758
Muneyuki Sakata
Tokyo Metropolitan Institute of Gerontology
Kenji Ishibashi
Tokyo Metropolitan Institute of Gerontology
Akira Hirayama
GE Healthcare
Hirofumi Kawakami
GE Healthcare
Kenta Miwa
International University of Health and Welfare
Yukihisa Suzuki
Tokyo Medical and Dental University
Kenji Ishii
Tokyo Metropolitan Institute of Gerontology

Original research

Keywords: silicon photomultiplier, photomultiplier tube, digital positron emission tomography, image quality, standardized uptake value ratio, statistical image analysis

Posted Date: April 30th, 2020

DOI: https://doi.org/10.21203/rs.3.rs-25131/v1

Version of Record: A version of this preprint was published at EJNMMI Physics on November 23rd, 2020.
See the published version at https://doi.org/10.1186/s40658-020-00337-4.

Abstract

Background

Silicon photomultiplier-positron emission tomography (SiPM-PET) has better sensitivity, spatial resolution, and timing resolution than photomultiplier tubes (PMT)-PET. The present study aimed to clarify the advantages of SiPM-PET in ^{18}F-fluoro-2-deoxy-D-glucose ([^{18}F]FDG) brain imaging in a head-to-head comparison with PMT-PET in phantom and clinical studies.

Methods

Image contrast was calculated from images acquired from a Hoffman 3D brain phantom and image noise and uniformity were calculated from pooled images acquired from a pool phantom using SiPM- and PMT-PET. Sequential PMT-PET and SiPM-PET [^{18}F]FDG images were acquired over a period of 10 min from 22 individuals. All images were separately normalized to a standard [^{18}F]FDG PET template, then mean standardized uptake values (SUV_{mean}) and Z-score were calculated by MIMneuro and Cortex ID Suite, respectively.

Results

Image contrast, image noise, and uniformity in SiPM-PET changed 27.5%, -2.1%, and − 138.2% from PMT-PET, respectively. These physical indices of SiPM-PET satisfied the criteria for acceptable image quality published by the Japanese Society of Nuclear Medicine of > 55%, ≤ 15% and ≤ 0.0249, respectively. The residual background count was reduced with time-of-flight algorithm especially in SiPM-PET. The SUV_{mean} using SiPM-PET was significantly higher than PMT-PET and did not correlate with a time delay. Z-scores were also significantly higher in images acquired from SiPM-PET (except for the bilateral posterior cingulate) than PMT-PET because the peak signal that was extracted by the calculation of Z-score in Cortex ID Suite was raised.

Conclusions

The better spatial and timing resolution, and sensitivity in SiPM-PET were contributed to better image contrast, image noise, and uniformity on brain [^{18}F]FDG images. SiPM-PET offers better quality and more accurate quantitation of brain PET images. The SUV_{mean} and Z-score in SiPM-PET was higher than PMT-PET. [^{18}F]FDG images acquired using SiPM-PET will help to improve diagnostic outcomes based on the statistical image analysis because the SiPM-PET was more localized the distribution of glucose metabolism on Z-score maps.

Introduction

Positron emission tomography (PET) has become an important imaging technology for evaluating biochemical and physiological functions and pathological abnormalities (1),(2). Brain imaging with ^{18}F-fluoro-2-deoxy-D-glucose ([^{18}F]FDG) measures local glucose metabolism as a proxy for neuronal activity, and thus is a powerful tool for differentially diagnosing dementia.

Silicon photomultipliers (SiPM) have replaced photomultiplier tubes (PMT) in newer PET detector systems. The features of SiPM comprise good intrinsic timing resolution (< 200 ps) and spatial resolution, compact, rugged design, higher gain (similar to that of PMT) and more sensitive photon detection than PMT. The first commercial SiPM-based PET/computed tomography (CT) was the Discovery MI (DMI; GE Healthcare, Milwaukee, WI, USA) that consisted of an axial field-of-view (FOV) of 20 cm, a small lutetium-based scintillators (LBS) with a SiPM block design, and timing resolution of 390 ps. We showed that the SiPM-PET had good sensitivity as well as spatial and timing resolution in National Electrical Manufactured Association (NEMA) performance tests. Contrast was better on images acquired from the DMI than the Discovery PET/CT 710 (D710, GE Healthcare) that had PMT detectors (3).

The clinical applicability of SiPM-PET/CT has been investigated. Hsu et al. found that SiPM-PET improved the contrast recovery of small lesions (4). Tiny malignant lesions in a patient with melanoma were detected on [^{18}F]FDG images acquired using SiPM-PET/CT and a Bayesian penalized-likelihood reconstruction algorithm (5). Sonni et al. reported that SiPM technology and time-of-flight (TOF) algorithm could reduce the duration of whole-body image acquisition without loss of the image quality (6). Salvadori et al. compared the image quality of brain [^{18}F]FDG images between Philips SiPM- and PMT-PET scanners (7). Image contrast, noise, and spatial resolution were better for images acquired using digital PET in their clinical study.

The present study aimed to clarify the advantage of SiPM-PET system in [^{18}F]FDG brain imaging in head-to-head comparisons between DMI and D710 in phantom and clinical studies. To our knowledge, this is the first attempt to evaluate the image quality with phantom study and quantitative value and the results of statistical image analysis with clinical study in SiPM-PET.

Materials And Methods

PET/CT systems

Discovery MI

The Discovery MI is a combination of LBS, an SiPM-PET scanner and a 64-slice CT scanner. The LBS includes four blocks of detectors aligned in the axial direction, each comprising 19,584 crystals (3.95 × 5.3 × 25-mm) in a 4 × 9 matrix. The scanner has 36 detector units per ring and 9,792 SiPM channels. The DMI enables axial and transaxial FOV of 20 and 70 cm, respectively, with 71 image planes spaced at

2.79-mm intervals. The spatial resolution according to NEMA NU 2-2012 is 3.91 mm at full width at half maximum (FWHM) (3).

Discovery PET/CT 710

The Discovery PET/CT 710 is a combination of LBS with PMT-PET and 64-slice CT scanners. The PET scanner has 13,824 LBS crystals in a 4.2 × 6.3 × 25-mm^3 block. The D710 enables a 150.42-mm axial FOV and a 700-mm transaxial FOV with 47 image planes spaced at 3.27-mm intervals. The timing resolution is 500 ps. The spatial resolution according to a NEMA NU 2-2007 was 4.52 mm at FWHM (8).

PET reconstruction condition

Data acquired using SiPM-PET and PMT-PET were reconstructed under the following conditions: three dimensional-ordered subset-expectation maximization (3D-OS-EM) with TOF; 4 iterations; 16 subsets; Gaussian filter, 2.5 mm (FWHM); 128 × 128 matrix size; FOV, 25.6 cm; 2.0 mm/pixel. The PET images of the Hoffman 3D brain phantom acquired by both scanners were reconstructed as described without TOF to evaluate TOF gain in background counts.

Phantom study

Data acquisition

Images from Hoffman 3D brain phantom (Data Spectrum Corporation, Hillsborough, NC, USA) and pool phantom (Itoi Plastics Co. Ltd., Kobe, Japan) containing 20 MBq of [^{18}F]FDG were acquired for 30 min in list mode using the SiPM-PET and PMT-PET systems. Phantom conditions and the scan duration were determined according to the Japanese Society of Nuclear Medicine (JSNM) phantom test procedure (9). We extracted a time frame of 0 – 7 min from 30 min of data derived from the Hoffman and pool phantoms that was equivalent to the count statistics for [^{18}F]FDG clinical brain images at the Tokyo Metropolitan Institute of Gerontology (TMIG) as described below.

Data processing

The physical indices for phantom tests proposed by the JSNM were used to evaluate the image quality: the ratio of grey-to-white matter contrast (contrast) calculated from images of Hoffman phantom, image noise (coefficient of variation, CV [%]) and uniformity (standard deviation, SD) calculated from images of pool phantom (9). The SD was also calculated from the pool phantom image with a scan duration of 30 min. The contrast, CV and SD were respectively calculated as described using images acquired from Hoffman and pool phantoms (9). Eight 10-mm circular volumes of interest (VOI) were placed on images of the acrylic plate at the bottom of the Hoffman phantom that were reconstructed using 3D-OS-EM with and without the TOF in the background (BG) (Fig. 1). The TOF gain (%) in the background counts was calculated as:

[Please see the supplementary files section to view the equation.] ,

where $BG_{non\text{-}TOF}$ *and* BG_{TOF} are mean background counts [kBq/mL] with and without TOF, respectively.

Clinical protocol

Data acquisition

The present study proceeded in accordance with the Declaration of Helsinki, and was approved by the Ethics Committee at the TMIG (Approval No. 28077). All applicants provided written informed consent to participate in the present study after physicians provided a detailed explanation of the study. The individuals rested comfortably in a quiet, dimly-lit room for several minutes, then were placed in the supine position for intravenous [^{18}F]FDG injection and uptake. Low-dose CT images for attenuation and scatter correction were acquired before starting PET image acquisition. The first set of PMT-PET images were acquired for 10 min starting from 40 min after [^{18}F]FDG administration, then the second set of SiPM-PET images was acquired, also for 10 min. We assessed 22 individuals using two PET/CT scanners between April 2017 and July 2018. Twenty two individuals were confirmed without degenerative neurological disorder on [^{18}F]FDG and brain magnetic resonance (MR) images acquired using a Discovery MR750w 3.0T scanner (GE Healthcare) in the three dimensional mode (spoiled gradient recalled acquisition in the steady state: repetition time, 7.648 ms; echo time, 3.092 ms; matrix size, 196 ×

256 × 256; voxel size, 1.2 × 1.0547 × 1.0547 mm^3). Table 1 shows the characteristics of these individuals who were cognitively normal. The 4 of 22 individuals were normal volunteer and 18 of 22 individuals had visual problem (visual snow, 12; blepharospasm, 2; visual disturbance, 1; photophobia, 1; Charles Bonnet syndrome, 1; traffic injury, 1).

Table 1. Characteristics of individuals (n = 22)

Age (y; minimum - maximum)	41.1 ± 18.9, (21-75)
Male (n)	11
Height (cm)	166.1 ± 7.5
Weight (kg)	58.5 ± 9.1
Glucose (mg/dL)	101.0 ± 13.7
Injected dose (MBq)	155.8 ± 14.7
Uptake duration (min, PMT-PET/SiPM-PET)	40.1 ± 0.6/55.3 ± 1.2

Data are shown as means ± standard deviation. PET, positron emission tomography; PMT, photomultiplier tube; SiPM, Silicon photomultiplier.

Data processing

All [^{18}F]FDG images were separately normalized to a standard [^{18}F]FDG PET and MR template using a MIMneuro (MIM Software Inc. Cleveland, OH, USA). Anatomical VOI of MIMneuro were automatically placed on the caudate nucleus, cerebellum, frontal, occipital, parietal and temporal lobes, putamen, thalamus and whole brain. Mean standardized uptake values (SUV_{mean}) were measured using these VOIs (10). Statistical image analysis was performed using Cortex ID Suite (GE Healthcare)(11-13). Cortex ID Suite includes original normal database, the VOI values of individuals and those of the normal database for were statistically compared. Anatomical VOI of Cortex ID Suite comprised the lateral and medial frontal, inferior and superior parietal, and lateral and medial temporal lobes, the anterior and posterior cingulate cortex, occipital lobe, sensorimotor, precuneus, primary visual cortex, and cerebellum.

The SUV ratio (SUVR) was calculated using the value of the pons as a reference region. Z-scores for anatomical VOI-based analyses were calculated from anatomically normalized SUVR images using the formula,

[Please see the supplementary files section to view the equation.] ,

where $SUVR_{individual}$ and $SUVR_{normal}$ are the mean SUVR of the individuals and the normal database in the VOI, respectively and SD_{normal} is the SD of the SUVR of the normal database in the VOI.

Data analyses

Data were statistically analyzed using GraphPad Prism 8 Version 8.4.0 (GraphPad Software Inc., San Diego, CA, USA). The SUV_{mean} of all regions for SiPM- and PMT- PET acquisitions were statistically compared using two-tailed paired Student *t* tests. Spearman rank correlation coefficients were calculated to evaluate relationships among different SUV_{mean} in the whole brain and intervals between acquisitions. Z-scores were statistically analyzed for both acquisitions using Wilcoxon matched-pairs signed rank tests. Values with $P < 0.05$ were considered significant.

Results

Phantom study

Table 2 shows that the physical indices of SiPM-PET satisfied the JSNM image quality acceptance criteria of contrast > 55%, CV ≤ 15% and SD ≤ 0.0249 (the clinical protocol at TMIG), whereas the contrast of PMT-PET images acquired for 7 min did not. The uniformity of the pool phantom images acquired for 7 min using SiPM-PET was also adequate. The BG count was dramatically reduced by using the SiPM-PET with TOF.

Table 2. Physical indices in JSNM criteria and TOF gain in background of SiPM- and PMT-PET.

	Contrast (%) (7 min)	CV (%) (7 min)	SD (7 vs. 30 min)	TOF gain (%) (7 min)
SiPM-PET	72.3	10.9	0.0157/0.0104	43.5
PMT-PET	52.4	11.1	0.0373/0.0186	10.0

JSNM criteria: contrast ratio > 55%, CV < 13%, SD < 0.0249. CV, coefficient of variation; JSNM, Japanese Society of Nuclear Medicine; PET, positron emission tomography; PMT, photomultiplier tube; SD, standard deviation; SiPM, silicon photomultiplier; TOF, time-of-flight.

Clinical study

Figure 2 and Table 3 show changes in SUV_{mean} and mean (± SD) SUV_{mean} across all brain regions, respectively, between acquired using SiPM- and PMT-PET. The SUV_{mean} was significantly higher on SiPM-PET than PMT-PET images in all region. The mean (± SD) of the interval between sequential acquisitions (PMT-PET followed by SiPM-PET) was 15.2 ± 1.0 min. The second acquisition started about 5 min after the end of the first acquisition. Figure 3 shows correlations between changes of SUV_{mean} in whole brain and time between first and second acquisitions. The *R* of the SUV_{mean} was 0.06 (*P* = 0.79), then the SUV_{mean} was independent of the time.

Table 3. Mean standardized uptake values for [^{18}F]FDG brain images acquired using SiPM- and PMT-PET (n = 22).

Region	PMT-PET	SiPM-PET	Difference
Cerebellum	5.5 ± 0.7	5.9 ± 0.7	7.9%
Brain stem	4.4 ± 0.5	4.6 ± 0.5	5.4%
Caudate	6.8 ± 1.3	7.4 ± 1.3	8.6%
Frontal lobe	6.6 ± 1.0	7.4 ± 1.1	11.0%
Occipital lobe	6.5 ± 0.9	7.5 ± 1.0	14.1%
Parietal lobe	6.2 ± 0.9	6.9 ± 1.0	11.9%
Temporal lobe	5.8 ± 0.8	6.6 ± 0.9	14.2%
Putamen	7.8 ± 1.1	8.5 ± 1.1	9.3%
Thalamus	6.9 ± 1.1	7.4 ± 1.1	7.2%
Whole brain	5.5 ± 0.8	6.1 ± 0.8	11.0%

Data are shown as means ± standard deviation. PET, positron emission tomography; PMT, photomultiplier tube; SiPM, Silicon photomultiplier.

Figure 4 shows that the comparisons of Z-scores that was analyzed using CotexID Suite in all regions (except the bilateral posterior cingulate) were significantly higher in SiPM-PET than PMT-PET images. Figure 5 shows [^{18}F]FDG images, Z-score maps, and MR images from an individual who was a 71-years-old male (number 9) with Charles Bonnet syndrome. The image of SiPM-PET was higher [^{18}F]FDG uptake at the grey matter than PMT-PET. The glucose metabolization was reduced at the visual association cortex on both statistical maps. The distribution of glucose hypometabolism was partially disappeared by using SiPM-PET (supplement 1).

Discussion

We validated the potential of a new digital SiPM-PET/CT system, DMI, by head-to-head comparisons with a conventional PMT-PET/CT system, D710, in phantom and clinical studies using [^{18}F]FDG imaging.

The phantom images acquired by SiPM-PET had less image noise and good uniformity. The voxel size of DMI ($2 \times 2 \times 2.79$ mm^3) was smaller than those of D710 ($2 \times 2 \times 3.27$ mm^3). The acquired PET count was normally higher in larger voxel size. However, the CV of SiPM-PET was slightly better than that of PMT-

PET. The SiPM-PET directly converts photons into a digital signal without signal loss and noise (6). The wider axial FOV of DMI was contributed to the better sensitivity in comparison with the D710 (200 vs. 157 mm) (3). For uniformity evaluation, the SD was calculated from mean radioactivity concentration at the center slice and on the slice ± 40 mm apart from the center of the pool phantom where were corresponded to the cerebellum (− 40 mm) and parietal lobe (+ 40 mm) in the human brain (9). Uniformity can be estimated as an index of the count stability through the entire axial FOV. Good uniformity means the less statistical noise on PET image at the edge of axial FOV. The SiPM-PET could include a whole brain within its PET axial FOV. The statistical noise was suppressed at the bottom of the brain such as pons and cerebellum where were the reference region to calculate the SUVR for [^{18}F]FDG (10), amyloid (14, 15), and Tau (16) PET imaging using the SiPM-PET. Therefore, the SUVR calculated by SiPM-PET was expected to be stable.

The SiPM-PET images acquired from Hoffman phantom had good image contrast and decreased residual BG counts due to good spatial and timing resolution. The improvement in image contrast (38.0%) were the same in the phantom study as that clinical study by Philips SiPM-PET (7). However, Salvadori et al. did not find a benefit of TOF with a digital PET system for brain PET (7). The timing resolution of the DMI and D710 was 375 and 544 ps, respectively(4, 8). These led to spatial localization along a line of response of 5.8 and 7.5 cm, respectively (3). The sensitivity gain using TOF was increased as a function of increasing the object size(17). Nagaki et al. found that contrast in [^{18}F]FDG brain imaging is not improved using the PMT-PET system at a timing resolution of 555 ps (18). The SiPM-PET with TOF improved image contrast even for small objects such as a human brain compared with a human body.

The clinical study showed that the SUV_{mean} was significantly higher using SiPM-PET than PMT-PET and did not correlate with the delay of the time from the injection (19). The superior spatial and timing resolution by SiPM-PET not only improved image contrast but also increased the SUV_{mean} in the cortex (2). The higher Z-scores determined using SiPM-PET was affected by higher SUV_{mean} and lower image noise. Cortex ID Suite uses the three-dimensional stereotactic surface projections (3D-SSP) as a method of statistical image analysis(11). The SiPM-PET raised the peak signal on the cortex that was used to analyze the 3D-SSP because small scintillator crystals in the SiPM-PET reduced the partial volume effects in the signal of grey matter (4). Salvadori et al. also found better recovery coefficient in SiPM-PET than PMT-PET even if same pixel size (7). The SiPM-PET that was higher Z-score might not detect the pathologic hypometabolism. However, the Z-score of bilateral primary visual cortex acquired both scanners was < 0 in present study. The distribution area of hypometabolism on Z-score maps using the SiPM-PET reduced and was localized (Fig. 5 and supplement 1). Thus, [^{18}F]FDG images acquired using SiPM-PET will help to improve diagnostic outcomes based on the statistical image analysis.

The present study has some limitations. First, we did not evaluate patients with neurological disorders. The detectability and diagnostic performance of SiPM-PET should be assessed among patients with neurological disorders. Second, twice acquisitions using SiPM- and PMT-PET were performed in specific

order. The sequential acquisition in inverse order should be performed to observe the actual change of SUV, although the SUV did not correlate with the delay of the time from the injection in present study. Third, Cortex ID Suite does not include image data acquired by the latest PET scanners such as the SiPM-PET in the original normal database. Z-scores determined using the SiPM-PET were tended to show higher value. If the original normal database of Cortex ID Suite is updated, the diagnostic performance using statistical image analysis is improved.

Conclusions

The better spatial and timing resolution, and sensitivity in SiPM-PET were contributed to better image contrast, image noise, and uniformity on brain [^{18}F]FDG images. The SiPM-PET offers better quality and more accurate quantitation of brain PET images. The SUV_{mean} and Z-score in SiPM-PET was higher than PMT-PET. [^{18}F]FDG images acquired using SiPM-PET will help to improve diagnostic outcomes based on the statistical image analysis because the SiPM-PET was more localized the distribution of glucose metabolism on Z-score maps.

List Of Abbreviations

[^{18}F]FDG, ^{18}F-fluoro-2-deoxy-D-glucose

3D-OS-EM, Three dimensional-Ordered Subset-Expectation Maximization

3D-SSP, Three-dimensional stereotactic surface projections

BG, Background

$BG_{non\text{-}TOF}$, Mean background counts without TOF

BG_{TOF}, Mean background counts with TOF

CT, Computed tomography

CV, Coefficient of variation

D710, Discovery PET/CT 710

DMI, Discovery MI

FOV, Field-of-view

FWHM, Full width at half maximum

Hoffman phantom, Hoffman 3D brain phantom

JSNM, Japanese Society of Nuclear Medicine

L, Left

LBS, Lutetium based scintillators

NC, Normal control

NEMA, National Electrical Manufactured Association

No., Number

PET, Positron emission tomography

PMT, Photomultiplier tubes

R, Right

ROI, Region of interest

SD, Standard deviation

SiPM, Silicon photomultiplier

SUV_{mean}, Mean standardized uptake value

SUVR, SUV ratio

TMIG, Tokyo Metropolitan Institute of Gerontology

TOF, Time-of-flight

VOI, Volume of interest

Declarations

Ethics approval and consent to participate and Consent for publication

The present study proceeded in accordance with the Declaration of Helsinki, and was approved by the Ethics Committee at the TMIG (Approval No. 28077). All applicants provided written informed consent to participate in the present study after physicians provided a detailed explanation of the study.

Availability of data and material

All data generated and analyzed during this study are included in this published article.

Competing interests

AH and HK are employed by GE Healthcare. KW, SM, and K Ishii were supported a research grant from GE Healthcare.

Funding

The design of the study, collection and analysis were supported by a research grant from GE Healthcare.

Authors' contributions

KW, AH, HK, and K Ishii designed the study. KW, K Ishibashi, YS, and K Ishii collected the data. KW and MS processed the data. KW, MS, KM, and K Ishii interpreted the data. KW drafted and revised the manuscript. All authors read and approved the final version of the manuscript.

Acknowledgements

We thank Mr. Shotaro Yamaguchi for technical support with the phantom experiment, Mr. Kunpei Hayashi and Mr. Masanari Sakai for technical support with the cyclotron operation and radiosynthesis, and Ms. Kimiko Yokoyama and Mr. Kazuno Hino for patient care as they underwent PET.

References

1. Wahl RL, Jacene H, Kasamon Y, Lodge MA. From RECIST to PERCIST: Evolving Considerations for PET response criteria in solid tumors. J Nucl Med. 2009;50 Suppl 1:122S-50S.
2. Lindstrom E, Sundin A, Trampal C, Lindsjo L, Ilan E, Danfors T, et al. Evaluation of Penalized-Likelihood Estimation Reconstruction on a Digital Time-of-Flight PET/CT Scanner for ^{18}F-FDG Whole-Body Examinations. J Nucl Med. 2018;59(7):1152-8.
3. Wagatsuma K, Miwa K, Sakata M, Oda K, Ono H, Kameyama M, et al. Comparison between new-generation SiPM-based and conventional PMT-based TOF-PET/CT. Phys Med. 2017;42:203-10.
4. Hsu DFC, Ilan E, Peterson WT, Uribe J, Lubberink M, Levin CS. Studies of a Next-Generation Silicon-Photomultiplier-Based Time-of-Flight PET/CT System. J Nucl Med. 2017;58(9):1511-8.
5. Aljared A, Alharbi AA, Huellner MW. BSREM Reconstruction for Improved Detection of In-Transit Metastases With Digital FDG-PET/CT in Patients With Malignant Melanoma. Clin Nucl Med. 2018;43(5):370-1.
6. Sonni I, Baratto L, Park S, Hatami N, Srinivas S, Davidzon G, et al. Initial experience with a SiPM-based PET/CT scanner: influence of acquisition time on image quality. EJNMMI Phys. 2018;5(1):9.
7. Salvadori J, Imbert L, Perrin M, Karcher G, Lamiral Z, Marie PY, et al. Head-to-head comparison of image quality between brain ^{18}F-FDG images recorded with a fully digital versus a last-generation analog PET camera. EJNMMI Res. 2019;9(1):61.
8. Bettinardi V, Presotto L, Rapisarda E, Picchio M, Gianolli L, Gilardi MC. Physical performance of the new hybrid PETCT Discovery-690. Med Phys. 2011;38(10):5394-411.

9. Akamatsu G, Ikari Y, Nishio T, Nishida H, Ohnishi A, Aita K, et al. Optimization of image reconstruction conditions with phantoms for brain FDG and amyloid PET imaging. Ann Nucl Med. 2016;30(1):18-28.
10. Partovi S, Yuh R, Pirozzi S, Lu Z, Couturier S, Grosse U, et al. Diagnostic performance of an automated analysis software for the diagnosis of Alzheimer's dementia with ^{18}F FDG PET. Am J Nucl Med Mol Imaging. 2017;7(1):12-23.
11. Minoshima S, Frey KA, Koeppe RA, Foster NL, Kuhl DE. A diagnostic approach in Alzheimer's disease using three-dimensional stereotactic surface projections of fluorine-18-FDG PET. J Nucl Med. 1995;36(7):1238-48.
12. Josephs KA, Duffy JR, Strand EA, Machulda MM, Senjem ML, Master AV, et al. Characterizing a neurodegenerative syndrome: primary progressive apraxia of speech. Brain. 2012;135(Pt 5):1522-36.
13. Probasco JC, Solnes L, Nalluri A, Cohen J, Jones KM, Zan E, et al. Abnormal brain metabolism on FDG-PET/CT is a common early finding in autoimmune encephalitis. Neurol Neuroimmunol Neuroinflamm. 2017;4(4):e352.
14. Joshi AD, Pontecorvo MJ, Lu M, Skovronsky DM, Mintun MA, Devous MD, Sr. A Semiautomated Method for Quantification of F 18 Florbetapir PET Images. J Nucl Med. 2015;56(11):1736-41.
15. Nelissen N, Van Laere K, Thurfjell L, Owenius R, Vandenbulcke M, Koole M, et al. Phase 1 study of the Pittsburgh compound B derivative ^{18}F-flutemetamol in healthy volunteers and patients with probable Alzheimer disease. J Nucl Med. 2009;50(8):1251-9.
16. Barret O, Alagille D, Sanabria S, Comley RA, Weimer RM, Borroni E, et al. Kinetic Modeling of the Tau PET Tracer ^{18}F-AV-1451 in Human Healthy Volunteers and Alzheimer Disease Subjects. J Nucl Med. 2017;58(7):1124-31.
17. Surti S. Update on time-of-flight PET imaging. J Nucl Med. 2015;56(1):98-105.
18. Nagaki A, Onoguchi M, Matsutomo N. Clinical validation of high-resolution image reconstruction algorithms in brain ^{18}F-FDG-PET: effect of incorporating Gaussian filter, point spread function, and time-of-flight. Nucl Med Commun. 2014;35(12):1224-32.
19. Baratto L, Park SY, Hatami N, Davidzon G, Srinivas S, Gambhir SS, et al. ^{18}F-FDG silicon photomultiplier PET/CT: A pilot study comparing semi-quantitative measurements with standard PET/CT. PLoS One. 2017;12(6):e0178936

Supplementary File Legend

Supplement 1: Z-score maps of bilateral and bimedial images in all individuals.

The color scale is -7.0 to 0.0 of Z-score. PET, positron emission tomography. PMT, photomultiplier tubes; SiPM, silicon photomultiplier.

Figures

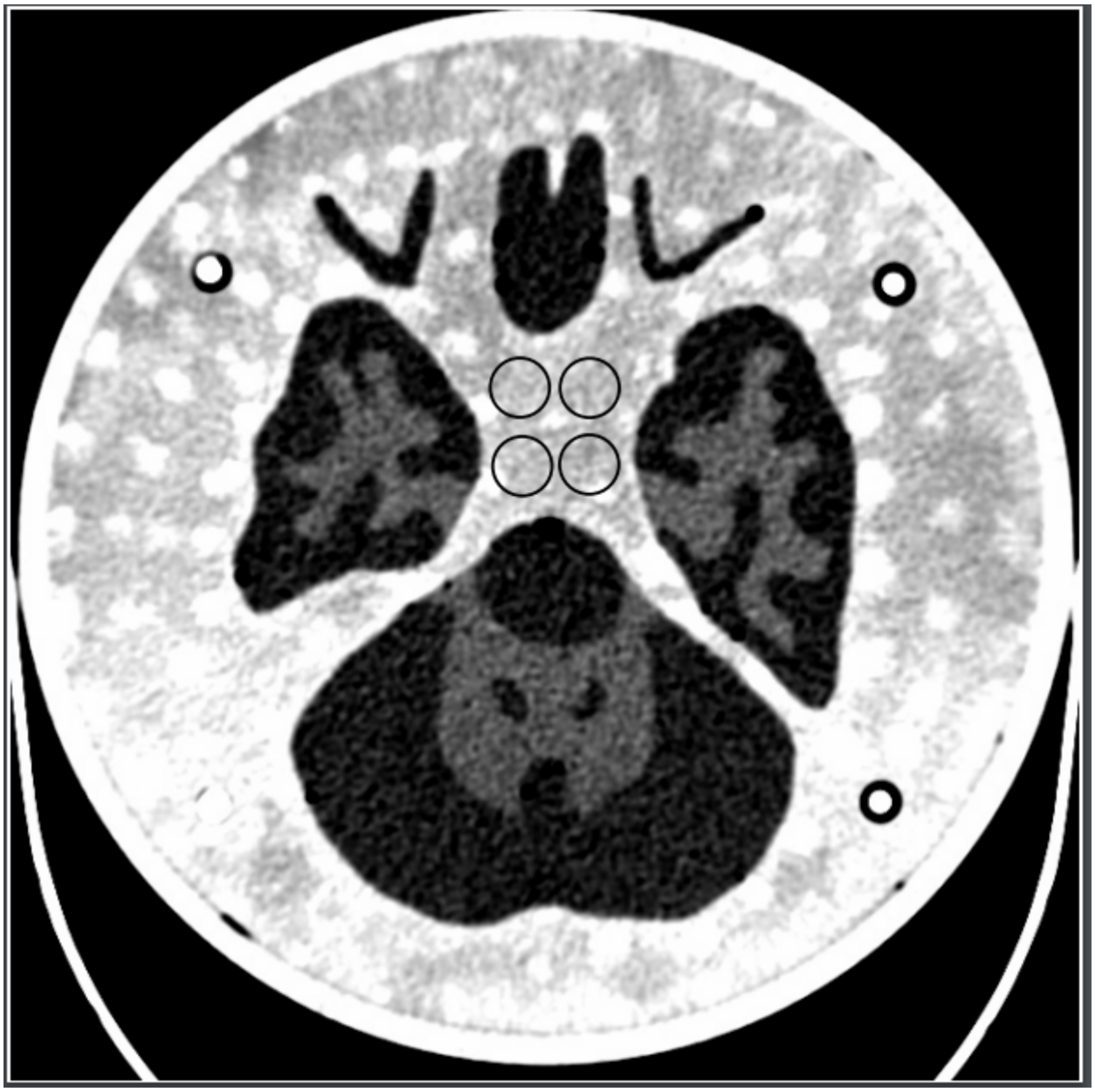

Figure 1

Position of circular ROI to measure background counts on bottom of Hoffman 3D brain phantom. Four circular ROI were placed on acrylic plate background and others were placed next to slices. ROI, regions of interest.

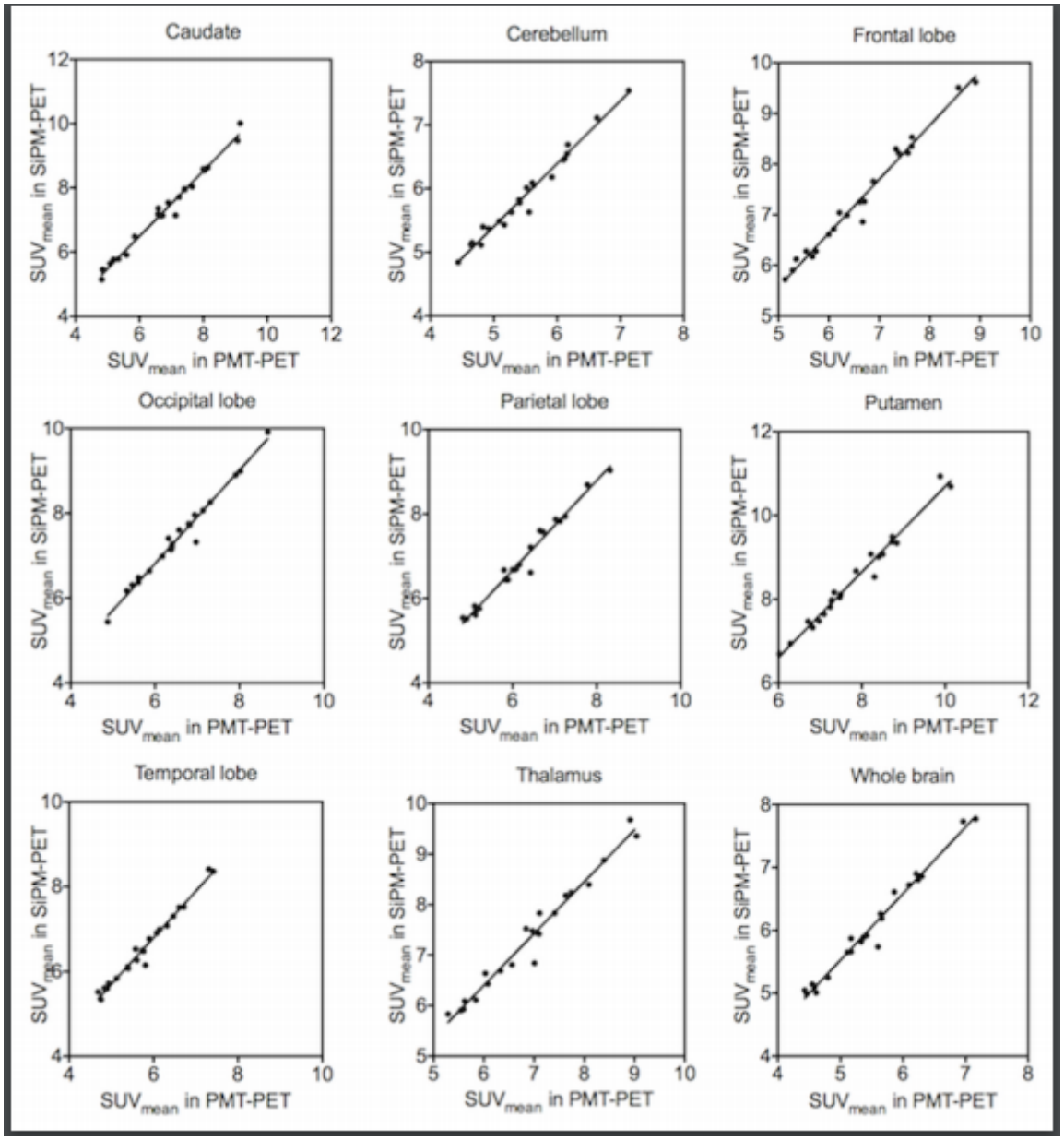

Figure 2

Changes in SUVmean of all regions in images acquired by PMT-PET and SiPM-PET. PET, positron emission tomography; PMT, photomultiplier tube; SiPM, silicon photomultiplier; SUVmean, mean standardized uptake value.

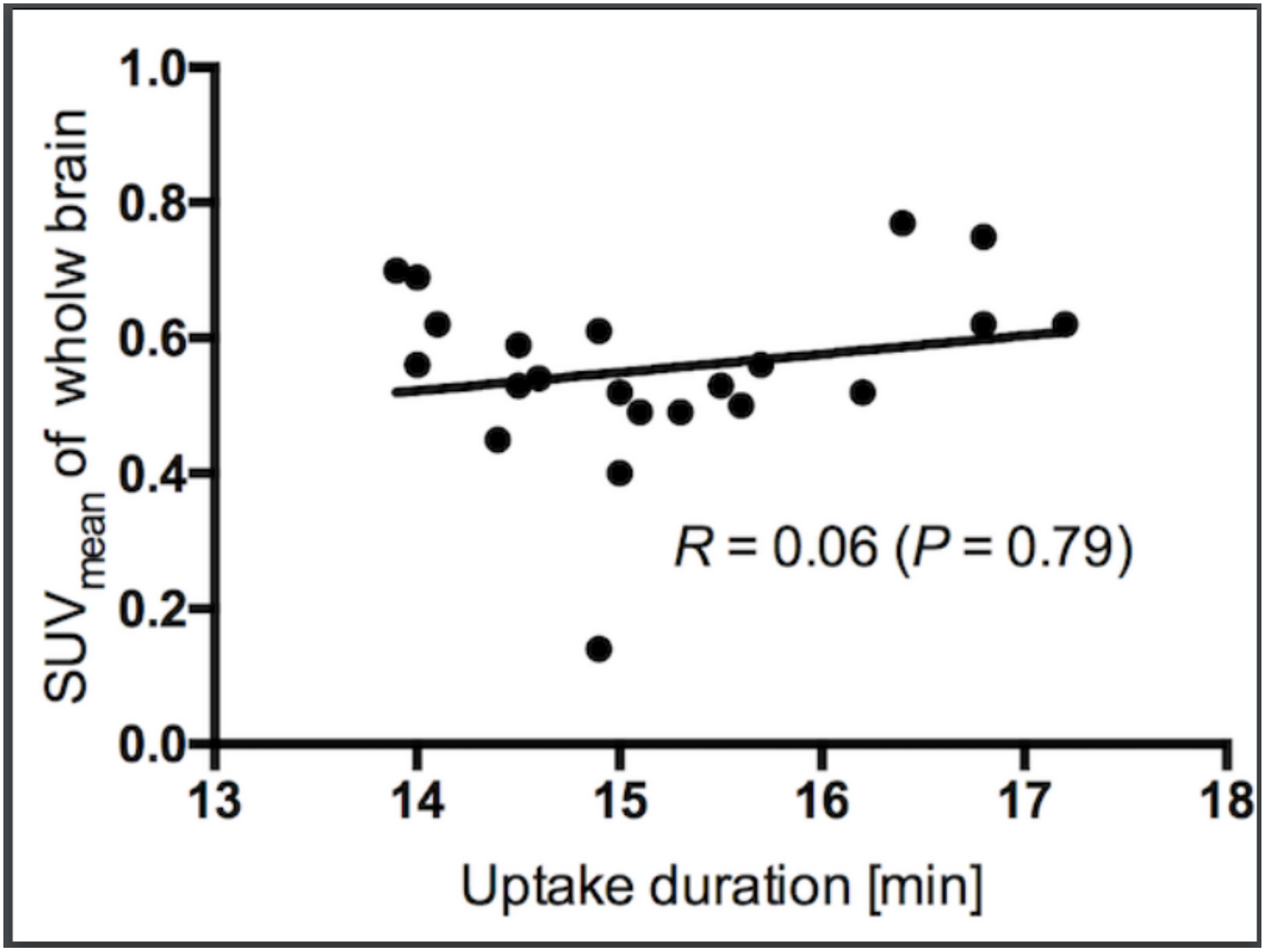

Figure 3

Correlations between changes in SUVmean in whole brain and time between sequential acquisitions. SUVmean, mean standardized uptake value.

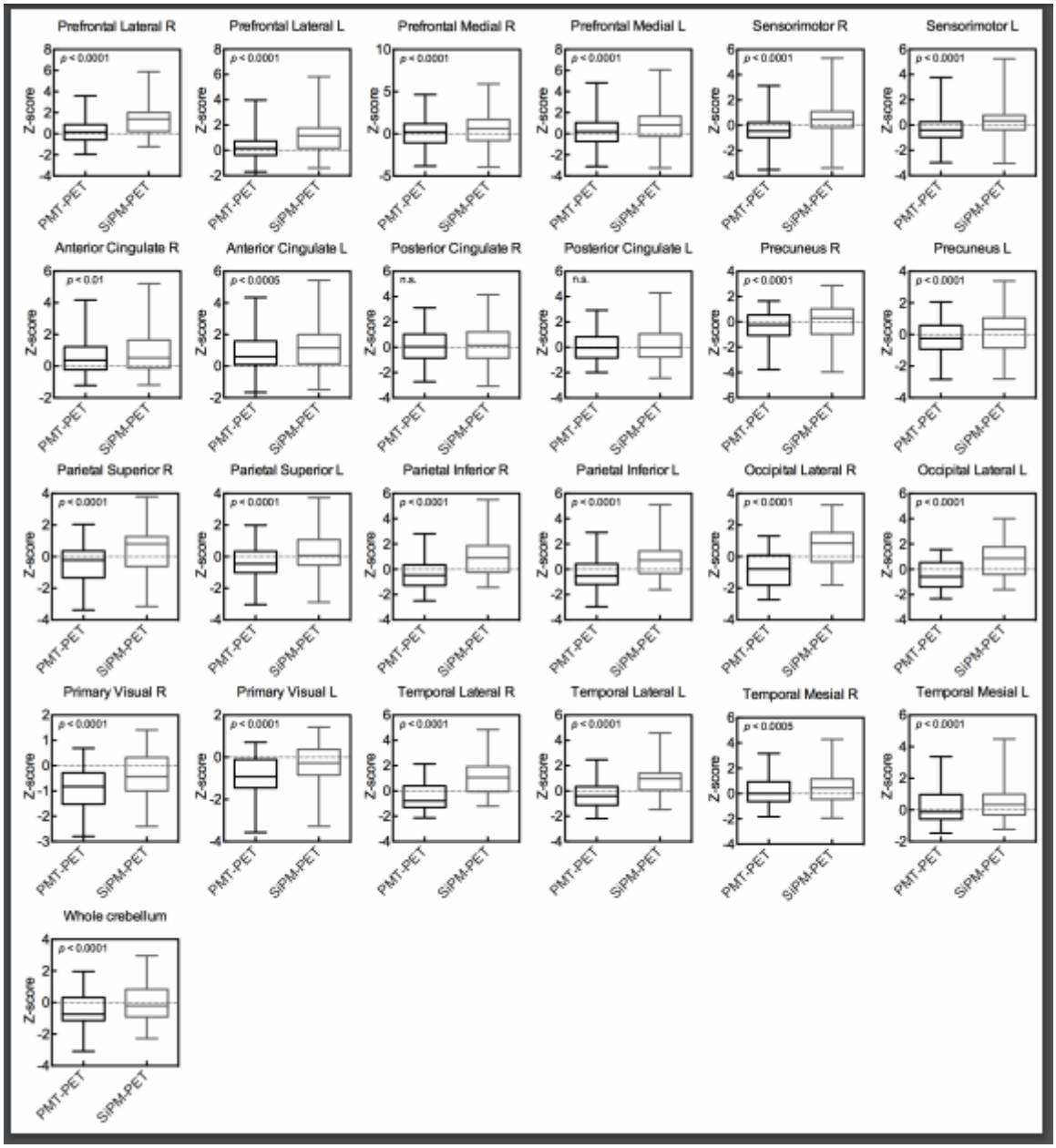

Figure 4

Z-scores in all brain regions in SiPM-PET and PMT-PET images. L, left; PET, positron emission tomography. PMT, photomultiplier tube; R, right; SiPM, silicon photomultiplier.

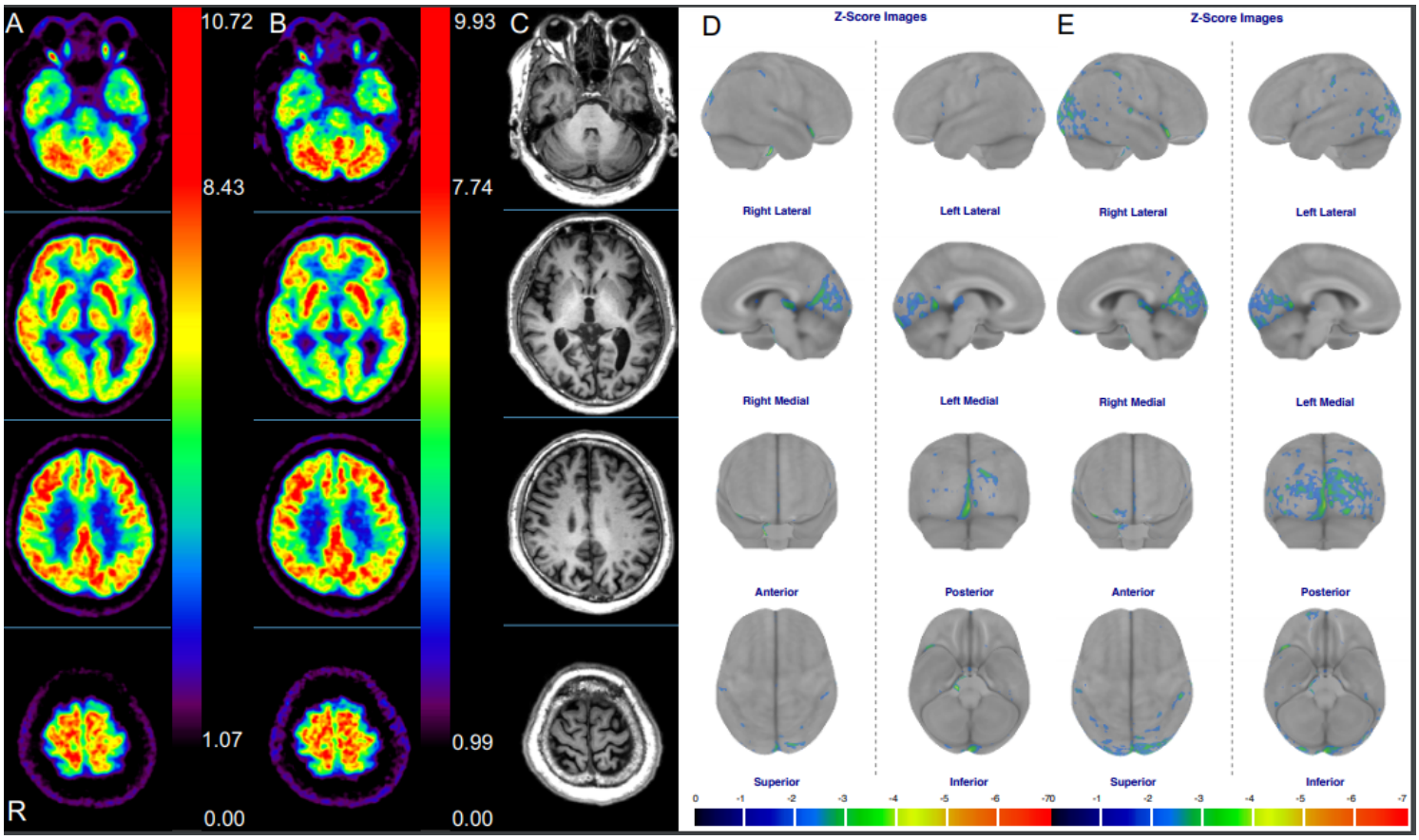

Figure 5

[18F]FDG images, MR images, and Z-score maps derived from a 39-year-old female. [18F]FDG images acquired using SiPM-PET (A) and PMT-PET (B). MR image of slices of both [18F]FDG images (C). Z-score maps calculated from SiPM-PET (D) and PMT-PET (E) images. MR, magnetic resonance; PET, positron emission tomography; PMT, photomultiplier tube; SiPM, silicon photomultiplier.

Supplementary Files

This is a list of supplementary files associated with this preprint. Click to download.

- Supplement1.pdf
- Equations.docx